

Improved representation of the contemporary Greenland ice sheet firn layer by IMAU-FDM v1.2G

Max Brils¹, Peter Kuipers Munneke¹, Willem Jan van de Berg¹, and Michiel van den Broeke¹

¹Institute for Marine and Atmospheric Research, Utrecht University, Utrecht, the Netherlands

Correspondence: Max Brils (m.brils@uu.nl)

Abstract.

The firn layer that covers 90% of the Greenland ice sheet (GrIS) plays an important role in determining the response of the ice sheet to climate change. Meltwater can percolate into the firn layer and refreeze at greater depths, thereby temporarily preventing mass loss. However, as global warming leads to increasing surface melt, more surface melt may refreeze in the firn layer, thereby reducing the capacity to buffer subsequent episodes of melt. This can lead to a tipping point in meltwater runoff. It is therefore important to study the evolution of the Greenland firn layer in the past, present and future. In this study, we present the latest version of our firn model, IMAU-FDM (Firn Densification Model) v1.2G, with an application to the GrIS. We improved the density of freshly fallen snow, the dry-snow densification rate and the firn's thermal conductivity using recently published parameterizations and by calibrating to an extended set of observations of firn density, temperature and liquid water content at the GrIS. Overall, the updated model settings lead to higher firn air content and higher 10 m firn temperatures, owing to a lower density near the surface. The effect of the new model settings on the surface elevation change is investigated through three case studies located at Summit, KAN-U and FA-13. Most notably, the updated model shows greater inter- and intra-annual variability in elevation and an increased sensitivity to climate forcing.

1 Introduction

Firn, the transitional stage between seasonal snow and ice in the accumulation zone of glaciers, strongly influences the climate response of mountain glaciers, ice caps and ice sheets. Pore space between snow grains that make up the firn layer enable meltwater to percolate into the firn layer, and refreeze – if the firn temperature is below freezing. This prevents runoff which means that firn acts as an efficient buffer against ice sheet mass loss. Diagnosing the current state of the Greenland ice sheet (GrIS) firn layer, and predicting its future, is therefore important in order to understand current and future changes in the mass balance of the GrIS.

A common method to assess the GrIS mass balance is altimetry, by which elevation changes are monitored by repeated scanning of the ice-sheet surface by active laser or radar instruments on board airplanes or satellites. A crucial step in translating the observed volume change to a mass change is to determine the density of the firn associated with the elevation change. To account for variability and changes in the surface mass balance and firn processes like compaction, percolation, and refreezing, a firn model is often employed for this step (Zwally et al. (2002); Sørensen et al. (2011); McMillan et al. (2016); Shepherd

et al. (2020); Hawley et al. (2020)). This is necessary since firn densification decreases the surface elevation without changing the mass balance, and is affected by changes in temperature and accumulation.

Firn models can also be used to assess the evolution of the aforementioned buffer capacity of the firn layer and how it is impacted by refreezing. It has been demonstrated that refreezing is a critical process for many ice caps to survive, e.g. in the Canadian Arctic. On these ice caps, summer melt consistently exceeds annual snowfall, and refreezing is required to maintain a near-zero mass balance (Noël et al. (2018a), Gascon et al. (2013); Bezeau et al. (2013); Ashmore et al. (2019)). As melt rates increase further in response to global warming, firn pore space is increasingly taken up by refrozen meltwater, degrading the efficiency of the refreezing process until at some point the available pore space has decreased to the extent that it cannot absorb all of the meltwater produced during summer. When this happens, the rate of mass loss increases irreversibly, which is why this is often regarded as a tipping point. At Greenland's marginal ice caps, this has already been taking place since the mid 1990s (Noël et al. (2017)).

Refreezing also plays an important role in the Greenland ice sheet (GrIS), but it has not yet reached this saturation tipping point (Pfeffer et al. (1991), Braithwaite et al. (1992)). The GrIS has an extensive firn layer ($\sim 1.4 \cdot 10^6$ km²), covering about 80% of the total area of the GrIS, which is higher in elevation (on average 2100 m above sea level (a.s.l.)) and hence more porous and colder than firn on other Arctic ice caps (Noël et al. (2020)). With a depth of up to 80 m (Kuipers Munneke et al. (2015b)), Vandecrux et al. (2019) estimated that the GrIS firn layer contains a total of 26800 ± 1840 km³ of air. This is equivalent to more than 60 times the total annual (1961-1990 average) volume of GrIS meltwater production (Van den Broeke et al. (2016)), although this is reduced to a factor of $\sim 1-4$ if only pore space in the percolation zone is considered (Harper et al. (2012)). Model estimates show that for the same period, at least 44% of the meltwater produced at the surface of the GrIS refroze in the firn layer (Van den Broeke et al. (2016); Mougnot et al. (2019)).

Surface melt is also increasing in the GrIS accumulation zone, with the extreme melt summers of 2012 and 2019 as vivid examples (Nghiem et al. (2012); Sasgen et al. (2020)). These high-melt summers led to peaks in refreezing, warming and densification of the firn layer (Steger et al. (2017a)). In some places, 1-2 m thick ice slabs were formed that prevent meltwater from reaching the pore space below (Machguth et al. (2016); MacFerrin et al. (2019)).

Lastly, firn models can be used to interpolate between observations (Kuipers Munneke et al. (2015b); Vandecrux et al. (2019)). This is convenient since observations from firn cores and snow pits are usually sparse and costly to obtain.

Some (regional) climate models are coupled interactively to a snow/firn model, but these often use simplified initialization, parametrizations and/or reduced vertical resolution for computational efficiency. The main advantage of using a dedicated, offline firn densification model is the lower computational cost, which enables the use of higher vertical resolution, a proper initialization of the firn layer, and extensive sensitivity testing (Lundin et al. (2017); Stevens et al. (2020); Vandecrux et al. (2020b)). The drawback of using an offline firn model is that it must be forced unidirectionally with observed and/or modelled surface temperature and surface mass fluxes (snow, rain, sublimation, drifting snow erosion).

In this study we present an updated version of the firn densification model of the Institute for Marine and Atmospheric research Utrecht (IMAU-FDM v1.2G, henceforth IMAU-FDM) applied to the GrIS, forced at the upper boundary by the latest

60 three-hourly output of the polar version of the Regional Atmospheric Climate Model (RACMO2, Noël et al. (2018b)). It supersedes the previous model version presented by Kuipers Munneke et al. (2015b) and Ligtenberg et al. (2018).

We use recently published parametrizations and previously existing and newly obtained observations of firn density, temperature and liquid water content from the GrIS to calibrate model parametrizations for surface (fresh snow) density, dry snow densification rate, thermal conductivity, and meltwater percolation. The updated model is subsequently used to perform case studies of contemporary firn depth variability in three climatologically distinct locations of the GrIS accumulation zone: (1) the dry and cold interior, (2) the relatively low-accumulation western percolation zone, and (3) the high-accumulation south-eastern percolation zone.

This paper is organized as follows: in Sect. 2 we describe the model details as well as the changes made to the model. We also describe the extended set of observations, both in time and space, that allows for new parametrizations and improved calibration of IMAU-FDM for the GrIS. Then, in Sect. 3, we show how the altered model results in an overall improved representation of GrIS firn density, temperature and liquid water content. The three case studies are then presented in Sect. 4, followed in Sect. 6 by a summary and outlook.

2 Methods

2.1 IMAU-FDM

75 For this work we use the offline IMAU-FDM, a semi-empirical firn densification model that simulates the time evolution of firn density, temperature, liquid water content and changes in surface elevation owing to variability of firn depth. The model has been compared extensively to, and calibrated with observations of firn density and temperature from the ice sheets of Greenland and Antarctica (Ligtenberg et al. (2011); Kuipers Munneke et al. (2015b); Ligtenberg et al. (2018)). IMAU-FDM is forced by three-hourly output of the polar version of the Regional Atmospheric Climate Model (RACMO2.3p2) (Noël et al. (2019)). Over glaciated grid cells, the RACMO2 subsurface model uses approximately the same expressions as IMAU-FDM, but with a lower vertical resolution (max. 150 vs. 3000 layers) and less comprehensive initialization to save computation time. For both the ice sheets of Greenland and Antarctica, the performance of IMAU-FDM has been comparable to the more physically-based SNOWPACK model (Steger et al. (2017b); Van Wessem et al. (2021); Keenan et al. (2021)). In the following subsections, we briefly describe how the main processes are currently represented in IMAU-FDM, and what improvements have been implemented compared to the previous model version.

2.1.1 Fresh snow density

An important boundary condition for the model is the density of freshly fallen snow, ρ_0 . When determined from field observations, fresh snow density is often assumed equal to the near-surface density, loosely defined as the average density of the top 0.5 m of dry snow. As density is highly variable near the surface, the exact chosen depth is critical for the outcome, which hampers a robust comparison between datasets (Fausto et al. (2018)). In firn models, fresh snow density is commonly parameterized as

a function of meteorological variables such as temperature and wind speed at the time of deposition, or, when these are not available, using annual average values instead (Keenan et al. (2021)). Several studies have addressed the parametrization of ρ_0 on the GrIS (Kuipers Munneke et al. (2015b); Fausto et al. (2018)). Assuming a linear dependence of the density on mean annual surface temperature T_s , this parametrization takes on the following form:

$$95 \quad \rho_0 = A + B \cdot T_s \quad (1)$$

With A and B being fitting constants and T_s in $^{\circ}\text{C}$. In previous studies where IMAU-FDM was applied to the GrIS, $A = 481 \text{ kg m}^{-3}$ and $B = 4.834 \text{ kg m}^{-3} \text{ K}^{-1}$ have been used (Kuipers Munneke et al. (2015b); Ligtenberg et al. (2018)) based on observations using the top 0.2 m average density from no-melt locations to approximate the surface value.

In the updated model, a new parameterization for fresh snow density (Fausto et al. (2018)) was adopted. In contrast to
100 previous studies, which typically use the first $\sim 0.5 - 1.0$ m of snow, Fausto et al. (2018) used only the upper 0.1 m of snow to define surface density at 200 locations and found:

$$\rho_0 = 362.1 + 2.78 \cdot T_a \quad (2)$$

with T_a the annual mean near-surface (usually 2 m) air temperature in $^{\circ}\text{C}$. Previously, the climatological mean 2 m air temperature has been used in IMAU-FDM (Kuipers Munneke et al. (2015a)), or an instantaneous value (Ligtenberg et al.
105 (2018)). In v1.2G of the model, T_a is calculated as the average 2 m air temperature of the year preceding the snowfall. While the actual density of fresh snow varies on much shorter time scales than this, we opt here for a parameterization that depends on annual mean surface temperatures for three reasons.

Firstly, the parameterization is derived by fitting the measured snow densities to mean annual temperatures, not the temperature at the time of the accumulation event. Thus the equation itself links snow density to annual temperatures, not instantaneous
110 temperatures. Therefore, using the instantaneous temperatures would introduce an additional uncertainty.

Secondly, in deriving their parameterization, Fausto et al. (2018) used the density of the upper 0.1 m of snow. Especially in locations where only a low amount of accumulation takes place, this means that the measured layer of firn contains snow from multiple accumulation events. Moreover, it may also have compacted in the time between the accumulation event and the observation. Therefore, we believe that the typical temperature to which this 0.1 m of snow is exposed to can more reasonably
115 be approximated with annual temperatures than with instantaneous ones.

Thirdly, using a climatological mean value suppresses the year-to-year variability in snow density. This is undesirable, especially because the model will also be used future scenarios, in which long term trends in temperature may have an effect. On the other hand, using instantaneous temperature values may introduce an excessive variability which, in reality, is smoothed by the effects of the snow being subjected to settling by wind and metamorphosis through numerous, daily warming and cooling
120 cycles. Calculating T_a in the updated model as the mean annual air temperature, is a trade-off between these two extremes that allows us to account for long term trends in air temperatures.

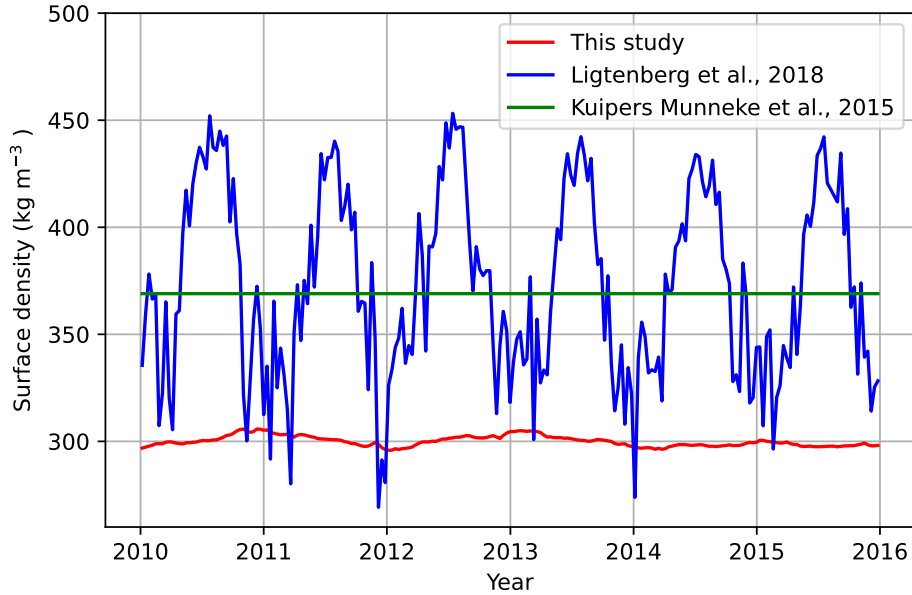


Figure 1. Daily averages of Das 2 (southeast Greenland, see Fig. 4) surface density (2010-2016) using three different parametrizations.

Fausto et al. (2018) noted that surface density correlates only weakly with annual mean T_a and that using a constant density of 315 kg m^{-3} may be preferable. Therefore, we compared the model's performance while using Eq. 2, with the model's performance while using a constant density of 315 kg m^{-3} . From this we concluded that neither configuration gives significantly better results. In Sect. 3.1 this comparison will be discussed in more detail.

Fig. 1 shows the surface density (2010-2016) using three different approaches at site Das 2 in Southeast Greenland. Clearly, temporal variations are much larger when an instantaneous T is used. Furthermore, the expression by Fausto et al. (2018) results in a lower surface density overall than Kuipers Munneke et al. (2015a). In subsequent sections, we refer to Ligtenberg et al. (2018) as for the previous model version.

130 2.1.2 Dry snow densification rate

IMAU-FDM is a 1D, vertical Lagrangian model. When new snow accumulates at the surface (model top), the model layers are buried deeper and tracked during their downward motion. At every time step, each layer is compacted under the influence of the pressure exerted by the mass of snow/firn above it. However, in IMAU-FDM the densification rate $\frac{d\rho}{dt}$ is not directly related to the overburden pressure, but rather follows a semi-empirical, temperature-dependent equation based on Arthern et al. (2010):

$$\frac{d\rho}{dt} = Cbg(\rho_i - \rho)e^{-\frac{E_c}{RT} + \frac{E_g}{RT_{ave}}} \quad (3)$$

where \dot{b} is the annual average accumulation rate (mm w.e. per year) over the spinup-period (1960-1979), $\rho_i = 917 \text{ kg m}^{-3}$ is the density of glacial ice, g , E_c , E_g and R are constants, and T is the instantaneous layer temperature in Kelvin. Different values of C above and below $\rho = 550 \text{ kg m}^{-3}$ represent a shift in the dominant densification mechanism (Cuffey and Paterson
140 (2011)). For $\rho < 550 \text{ kg m}^{-3}$, the densification of the firm is dominated by the settling and sliding of grains. For $\rho \geq 550 \text{ kg m}^{-3}$ recrystallisation, deformation and sublimation become dominant and the densification rate is lower, which is reflected in a lower value for C .

Arthern et al. (2010) base their densification rate on an equation describing Nabarro-Herring creep from Coble (1970). This rate depends linearly on the overburden pressure. The overburden pressure $\sigma(t)$ on a layer of firm of age t_{age} , is equal
145 to $\sigma(t_{age}) = g \int_{t-t_{age}}^t \dot{b}(t') dt'$ in the absence of melt. The accumulation rate enters the equation for the densification rate through the assumption that the accumulation rate is constant in time, replacing $\sigma(t)$. RACMO2 provides the average annual accumulation rate \dot{b} as the amount of total precipitation minus sublimation and drifting snow erosion during the spin-up period. Assuming a constant \dot{b} introduces an error in the load experienced by a layer of firm ($\sigma(t_{age}) = g\dot{b}t$). However, over the time scale considered here the error remains small (e.g. $< 3.2\%$ at Summit and $< 1.9\%$ at Dye-2).

Eq. 3 is used for both wet and dry locations, and so it is assumed that the densification rate of dry firm is equal to that of
150 wet firm. We acknowledge that the presence of liquid water in between grains may impact the evolution of their size and shape. This in turn may also impact the densification rate of the firm. Most firm models that account for a different densification rate of wetted firm are based of Vionnet et al. (2012). They introduce this dependency through an empirical correction factor for the firm viscosity. This correction factor is derived from experiments that have not been published (see Brun et al. (1992)). Due to
155 a lack of physical understanding and a lack of available measurements we decided not to introduce an extra dependence of the compaction rate on the liquid water content to reduce the model's complexity and to prevent overfitting.

Compared to observations of the depth of the 550 and 830 kg m^{-3} density levels, a structural bias is found when using
Eq. 3, that in previous studies turned out to depend on the annual average accumulation rate. In order to calibrate Eq. 3 to
the new, expanded set of observations, we introduce a multiplication factor MO to better align modelled density profiles with
160 observations:

$$\text{MO} = \alpha - \beta \ln(\dot{b}) \quad (4)$$

where α and β are unitless constants. Although the physical processes underlying the densification of firm do not explicitly
depend on the accumulation rate, a correlation between $\frac{d\rho}{dt}$ and \dot{b} may act as a proxy variable for effects that are time dependent,
possibly related to the geometry of grains (Cuffey and Paterson (2011)). Firm densification owing to horizontal compression is
165 neglected, although in fast-flowing regions this can be locally important (Horlings et al. (2021)).

In the model update, we recalibrated the dry densification correction factor MO as a function of mean annual accumulation,
by using an updated, high-resolution GrIS accumulation field (Noël et al. (2015)) and optimizing the modelled depths at which
the firm density reaches the critical values $550/830 \text{ kg m}^{-3}$ following Ligtenberg et al. (2011) and Kuipers Munneke et al.
(2015b). To perform the previous calibration, we expanded the 22-core data set by Kuipers Munneke et al. (2015b) to 29 cores.

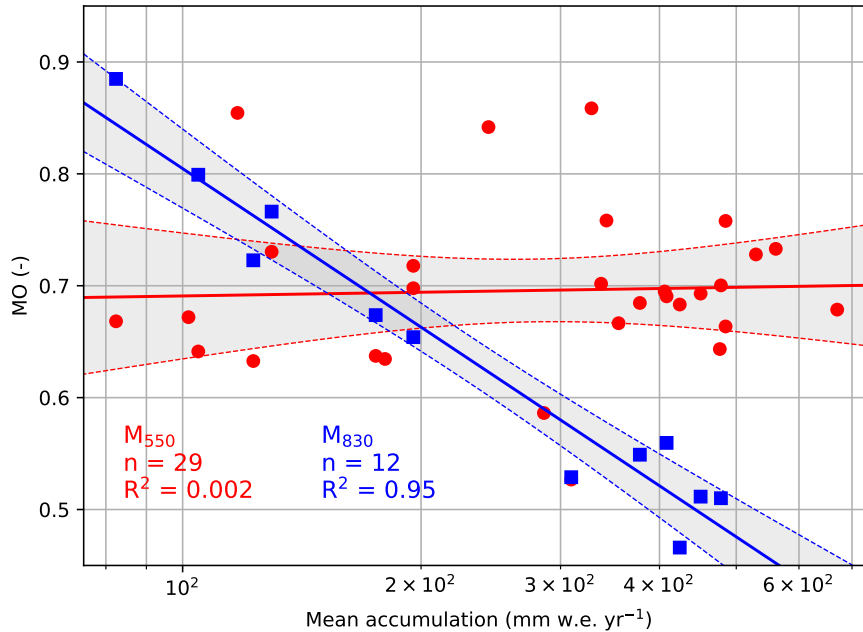


Figure 2. Ratio between modelled and observed depth at which the density reaches 550 kg m^{-3} (MO_{550}) or 830 kg m^{-3} (MO_{830}) as a function of local accumulation rate. The solid lines represent the corresponding regressions and the grey bands around them are their corresponding 95% confidence intervals.

170 Only dry firn cores (i.e. with little surface melt) are used for calibration. No "wet" cores are used since Eq. 3 only describes the densification rate due to overburden pressure. At wet locations, the density at a given depth is not only impacted through compaction by overburden pressure but also through the vertical transport of liquid water inside of the firn after a melt event. This drastically alters the depth at which the firn layer reaches 550 or 830 kg m^{-3} . Incorporating these ratios of depths into the derivation of the MO fit would incorrectly assign this change to a different compaction rate whereas it is due to refreezing. A
 175 core is considered as "dry" if the mean annual melt is less than 5% of the mean annual accumulation rate. Least squares fitting yields R^2 values for MO_{550} and MO_{830} of $1.57 \cdot 10^{-3}$ and 0.95 respectively. Fig. 2 shows the new calibrations. The statistics of the new fit are summarised in Table 1, along with the old values from Kuipers Munneke et al. (2015b). The standard error of the coefficients is calculated by assuming that the errors in the regression are normally distributed.

With the update and the use of new firn and accumulation data, the linear relation between MO_{550} and $\ln(\dot{b})$ vanishes, and
 180 reduces to an almost constant value of 0.67. Despite the difference with previous formulations in IMAU-FDM, this is similar to findings by Robin (1958) and Herron and Langway (1980), who also found that for densities lower than 550 kg m^{-3} the densification rate correlates almost linearly with accumulation, and that this correlation becomes non-linear at higher densities. The high correlation for MO_{830} also implies that the relation between densification rate $\frac{d\rho}{dt}$ and accumulation is non-linear above $\rho = 550 \text{ kg m}^{-3}$. We run the model with the newly derived values for α and β for MO_{550} and MO_{830} listed in Table 1.

Table 1. Values of the old and new linear regression of Eq. 4, their R^2 as well as the standard error in of the new fitting parameters.

	α_{old}	α_{new}	σ_α	β_{old}	β_{new}	σ_β	R_{old}^2	R_{new}^2
MO ₅₅₀	1.042	0.6688	0.1317	0.0916	-0.0048	0.0233	0.35	0.002
MO ₈₃₀	1.734	1.7465	0.0841	0.2039	0.2045	0.0154	0.96	0.946

185 2.1.3 Thermal conductivity

In IMAU-FDM, the vertical temperature distribution and its evolution is obtained by solving the one-dimensional heat transfer equation

$$\rho c \frac{\partial T}{\partial t} = -\frac{\partial G}{\partial z} + \mathcal{L} = -\frac{\partial}{\partial z} \left(k \frac{\partial T}{\partial z} \right) + \mathcal{L} \quad (5)$$

in which c is the specific heat capacity of the firm, G the diffusive ground heat flux, k the thermal conductivity of the firm and \mathcal{L} a heat source representing the release of latent heat upon the refreezing of liquid water in the firm or the subsurface absorption of solar radiation. Subsurface penetration of short-wave radiation is neglected in the current model version. This is deemed a reasonable approximation for fine-grained, polar snow (van Dalum et al. (2020)); Brandt and Warren (1993) showed that most of the absorption of light occurs in the IR and in the first few centimetres of the snow. The firm temperature profile is initialized using a spin-up period, see Sect. 2.1.5. Before the spin-up, the firm column is initialised at a constant temperature equal to the annual mean surface temperature during the spin-up period. The lower boundary condition assumes a constant heat flux across the lowest model grid cell, i.e. the deep temperature is allowed to change along with long-term changes in surface temperature or internal heat release. The upper boundary condition for the temperature calculation is provided by the surface ('skin') temperature in RACMO2, obtained by iteratively solving the surface energy balance (Van den Broeke et al. (2008)). Due to the Lagrangian character of the model, vertical heat advection is implicitly considered (Helsen et al. (2008)). Any heat generated by firm horizontal/vertical deformation is neglected.

The heat equation is solved numerically using the so called "splitting method". In the first half of a time step we solve for water transport using the bucket-scheme (described in more detail in the Sect. 2.1.4). Temperature changes caused by the refreezing of meltwater are added as a source term. Then, in the second half of the time step, no water flux is allowed, making every layer a closed system. We then allow heat conduction to take place by solving Eq. 5 implicitly using the Crank-Nicolson scheme.

The thermal conductivity is assumed to depend on firm density and temperature, and in previous versions of IMAU-FDM followed the expression for seasonal snow due to Anderson (1976), which only depends on density. In the updated model, the parameterization for thermal conductivity as a function of firm density of Calonne et al. (2019) is used. The new expression more accurately models the dynamics of the thermal conductivity by incorporating both a density and temperature dependency. The new expression was obtained from 3D images of firm micro-structures at different temperatures, and is valid for the wide

range of density and temperature values typically encountered in ice sheet firn layers, making it suitable for simulations of the GrIS. It takes on the following form:

$$k(\rho, T) = (1 - \theta) \frac{k_i(T)k_a(T)}{k_i(-3^\circ\text{C})k_a(-3^\circ\text{C})} k_{snow}(\rho) + \theta \frac{k_i(T)}{k_i(-3^\circ\text{C})} k_{firm}(\rho) \quad (6)$$

The equation consists of two parts: one for snow and low-density firn and one for ice and high-density firn. The transition between the two regimes remains smooth through the weight factor $\theta(\rho)$. The definition of θ and the thermal conductivities that are used in Eq. 6 are:

$$\theta = 1/(1 + \exp(-0.04(\rho - 450)))$$

$$k_i(T) = 9.828 \exp(-0.0057T)$$

$$k_a(T) = (2.334 \cdot 10^{-3} T^{3/2}) / (164.54 + T)$$

$$k_{snow}(\rho) = 0.024 - 1.23 \cdot 10^{-4} \rho + 2.5 \cdot 10^{-6} \rho^2$$

$$k_{firm}(\rho) = 2.107 + 0.003618(\rho - \rho_i)$$

Here k_a represents the thermal conductivity of air, taken from Reid et al. (1959). Figure 3 compares the old and new expressions for various temperatures. As can be seen in Fig. 3, the new expression takes on a slightly lower value than Anderson (1976) at densities below $\sim 475 - 565 \text{ kg m}^{-3}$, depending on the temperature, but a higher value at densities above that. This difference becomes larger at lower temperatures.

2.1.4 Meltwater percolation, retention and refreezing

IMAU-FDM employs a tipping bucket method to treat the percolation, irreducible (capillary) retention and (re)freezing of water, by filling up subsequent deeper layers to maximum capacity in a single model time step (i.e. quasi-instantaneous). Magnusson et al. (2015) show that, in spite of its simplicity and shortcomings, the tipping bucket method is a robust and useful method to deal with liquid water transport in the snowpack when compared to more sophisticated methods, especially when capturing general firn properties at the larger, multi-kilometre horizontal scale for which IMAU-FDM is designed. In IMAU-FDM, the fraction that is retained in a model layer by capillary forces ('irreducible water content') depends on the available pore space according to the expression by Coléou and Lesaffre (1998):

$$W_c = 1.7 + 5.7 \frac{P}{1 - P} \quad (7)$$

where W_c is the irreducible water content in percents of volume and P is the porosity of the firn layer, defined as $P = 1 - \rho/\rho_i$. The maximum amount of water that is stored thus decreases with increasing density of the firn layer. Standing water and as a consequence lateral runoff over ice-layers are currently ignored. This is considered a fair assumption, because on the

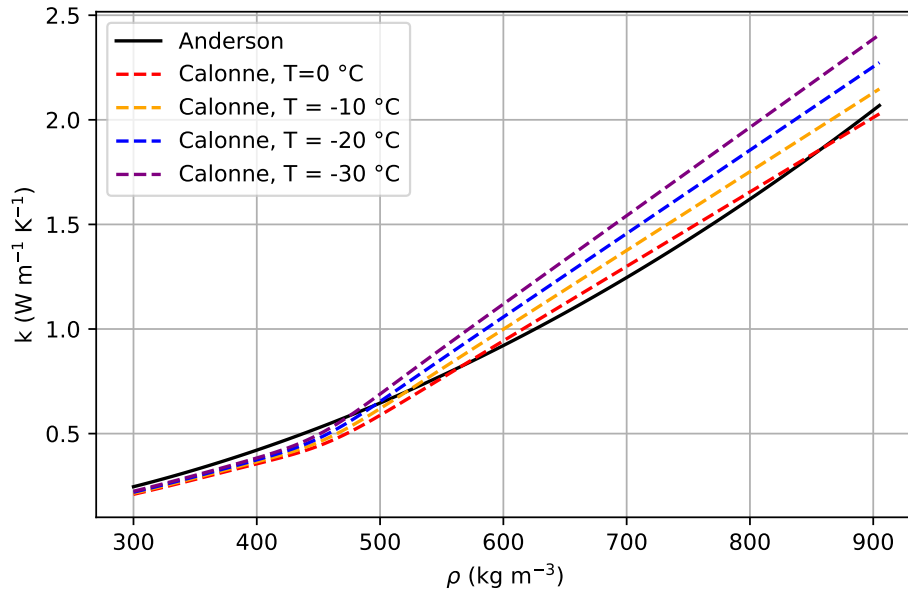


Figure 3. Comparison of the thermal conductivity parameterisation by Anderson (1976) and Calonne et al. (2019) with density at different temperatures.

spatial scales at which the model is employed (i.e. the RACMO2 grid of 5.5 by 5.5 km) it is assumed that within a model grid cell the meltwater can usually find a way to flow around a layer of ice.

240 2.1.5 Model initialisation

The latest IMAU-FDM model runs span the period 10 November 1957 - 31 December 2020. The initial model density, temperature and liquid water content in the firm column are obtained by repeatedly applying the spin-up period 1960 - 1979 during which the forcing (i.e. surface accumulation, liquid water flux and temperature) is assumed to have remained reasonably constant (i.e. no significant long-term trends, Van den Broeke et al. (2009)). Observations and model studies support the assumption that the Greenland climate and SMB started to change significantly in the 1990s (Enderlin et al. (2014); McMillan et al. (2016)), confirming that the period 1960 - 1979 can be selected for initialization purposes. Initialization is considered complete when the entire firm layer (up to the pore close-off density of 830 kg m⁻³) has been refreshed. The required number of iterations depends on accumulation rate, and is typically 25 to 45 for the relatively dry grid points in the northeastern GrIS and typically 10 to 20 for the relatively wet southeastern GrIS. After the spin-up is finished, the actual model run starts by applying the 1957-2020 forcing from RACMO2.3p2 once.

2.2 RACMO2.3p2 forcing

At the upper boundary of IMAU-FDM, mass accumulation (solid precipitation minus sublimation minus drifting snow erosion), liquid water fluxes (melt plus rainfall minus evaporation) and surface temperature are prescribed from the regional atmospheric climate model RACMO2.3p2, which has been used to simulate the climate and surface mass balance of the GrIS and its immediate surroundings for the period 1958-2020 at a horizontal resolution of 5.5 km. Like previous versions, this version of RACMO2 has been extensively evaluated over the GrIS (Noël et al. (2018b)). At the lateral boundaries, using a relaxation zone of 24 gridpoints, RACMO2 is forced by European Centre for Medium-Range Weather Forecasts (ECMWF) re-analysis data, i.e. ERA-40 between November 1957 and 1978, ERA-Interim between 1979 and 1990 and ERA-5 between 1991 and 2020. For the forcing of IMAU-FDM the full spatial resolution of 5.5 km is used and a temporal resolution of 3 hours was selected, as an acceptable trade-off between robustly resolving the daily cycle and keeping manageable file sizes. IMAU-FDM typically uses a timestep of 15 min, for which we linearly interpolate the forcing between the RACMO2 forcing time steps.

2.3 Firn thickness and elevation change

IMAU-FDM tracks the total firn thickness, and changes in it. The resulting vertical velocity of the ice-sheet surface due to changes in the firn layer ($\frac{dh}{dt}$) is given by:

$$\frac{dh}{dt} = v_{snow} + v_{snd} + v_{er} + v_{melt} + v_{ice} + v_{fc} \quad (8)$$

The total vertical surface velocity $\frac{dh}{dt}$ can thus be decomposed into separate contributions from accumulation (v_{snow}), surface sublimation (included in v_{snow}), sublimation by snowdrift (v_{snd}), erosion or deposition by snowdrift (v_{er}), snowmelt (v_{melt}), and firn compaction (v_{fc}). The term v_{ice} is defined as the mean surface mass balance (SMB, $v_{ice} = v_{snow} + v_{snd} + v_{er} + v_{melt}$) with an opposite sign. It represents the long-term average vertical mass flux through the lower boundary of the firn column, which equals the mass flux through the upper boundary in a steady-state firn layer. In Sect. 4 we show surface elevation change and the individual components for three case study locations on the GrIS.

2.4 Observations

IMAU-FDM output is evaluated using previously available and newly obtained profiles of firn density, temperature and liquid water content from the GrIS accumulation zone. The 123 observations cover a wide area to ensure that the various ice facies and climate zones of the GrIS are well represented (Fig. 4). Vertical profiles of observed firn density from ice cores vary in depth from 9.6 to 150.8 m and have been drilled between 1952 and 2018. The cores come from various sources, such as the Program for Arctic Regional Climate Assessment (PARCA; McConnell et al. (2000); Mosley-Thompson et al. (2001); Hanna et al. (2006); Banta and McConnell (2007)), the Arctic Circle Traverses (ACT, Box et al. (2013)) and the EGIG line (Harper et al. (2012)), Das 1 and Das 2 (e.g. from Hanna et al. (2006)) and several other cores were retrieved from the SUMup database (Surface Mass balance and snow depth on sea ice working group), (Koenig et al. (2013); Montgomery et al. (2018)). Table S1

in the supplementary material lists all cores that have been used, their coordinates, the year in which it has been drilled, depth and corresponding citation.

Temperature observations include profiles ranging in depth between 4 and 14 m obtained by Harper et al. (2012) along a transect in the western GrIS and at the NEEM deep ice core drilling site (Orsi et al. (2017)). Additional firn temperature
285 observations are from Summit, Dye-2 (Steffen et al. (1996) as processed by Vandecrux et al. (2020a), KAN-U (Charalampidis et al. (2015)) and FA-13 (Koenig et al. (2014)). An additional 14 observations of 10 m firn temperatures are from Polashenski et al. (2014). More data concerning these observations, such as their coordinates and year of retrieval, is listed in Table S2 of the supplementary material.

For observations of liquid water in firn, we use observations from Dye-2 (Heilig et al. (2018)), obtained using an upward-
290 looking ground-penetrating radar (upGPR), which was installed and operated in the summer of 2016. The upGPR was buried ~ 4.5 m under the snow, and was capable of measuring the liquid water percolation depth, content as well as the changing distance between the instrument and the snow surface. Although the data do not cover a wide spatial (single location) or temporal range (1 May-16 October 2016), they are unique and moreover have high temporal and vertical resolution, making them very valuable for firn model evaluation (Vandecrux et al. (2020b)), but also to evaluate melt intensity and timing in the
295 forcing time series.

3 Model performance

3.1 Firn density

The vertical density profiles of 92 GrIS firn cores are used to assess the performance of the updated model. For each available firn core, IMAU-FDM has been run at the grid point closest to that location. The evaluation is not completely independent
300 of the calibration, as the 29 cores used for fitting the MO-values are also included. As an integrated measure of porosity, we compare modelled and observed vertically integrated firn air content (FAC), i.e. the vertical distance over which the firn layer can be compressed until reaching the density of glacier ice across the entire firn column. FAC is an indicator of the meltwater retention capacity of the firn layer and therewith an important parameter to simulate correctly.

$$\text{FAC} = \sum_j^{n_z} \frac{(\rho_i - \rho_j)}{\rho_i} \Delta z_j \quad (9)$$

305 Here, n_z is the number of layers in that firn profile, Δz_j is the thickness of layer j and ρ_j is the density of that layer. The FAC is calculated over the depth range at which observations are available. This means that if, for example, a core goes up to a depth of 20 m then the FAC is calculated over the top 20 m, but if a different core is 40 m deep then the FAC for that data point FAC is calculated over the top 40 m of firn. Note that this is different from FAC_{10} shown in Fig. 4, which was calculated over the top 10 m. This ensures that we compare the FAC with observations over the largest depth range possible. In general,
310 the more melt a location on the GrIS experiences the lower its FAC and shorter firn cores obviously also lead to a lower FAC.

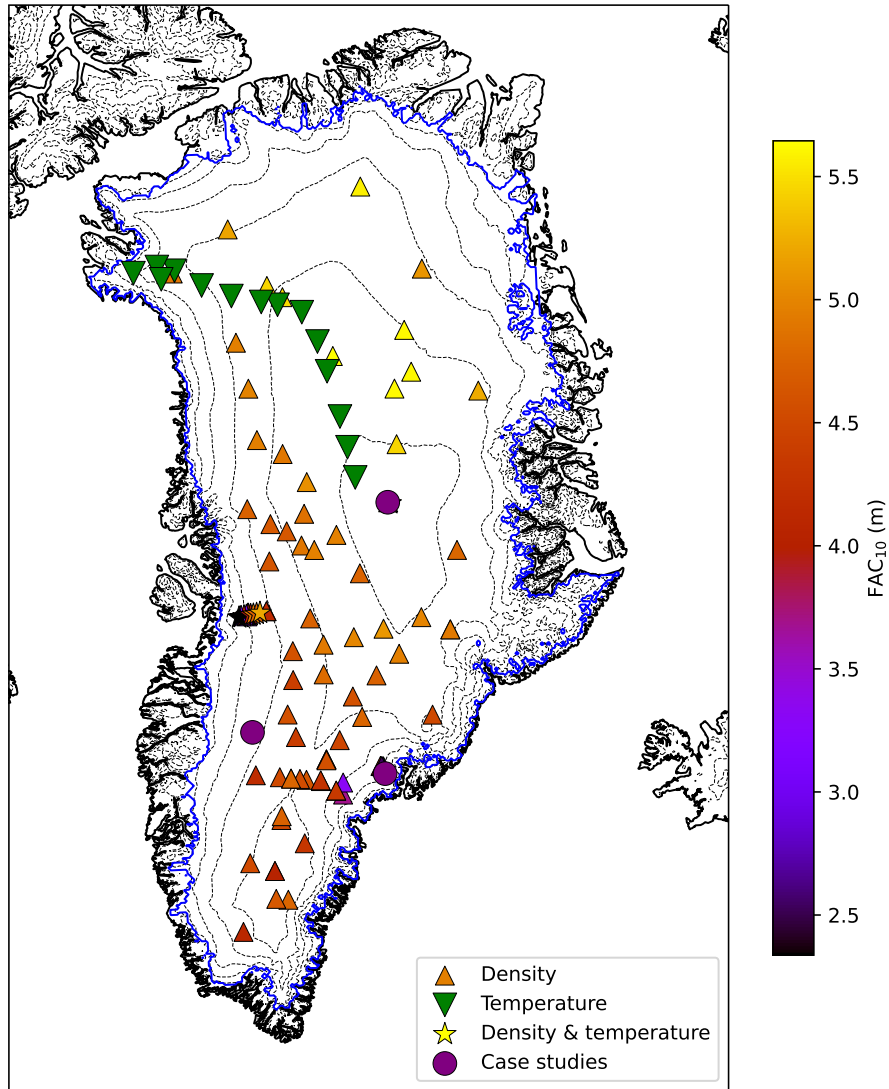


Figure 4. Locations of observed density (upward triangle), 10 m temperature (downward triangle), both (stars). The colour of the upward triangles and stars indicate the measured firn air content for the first 10 m of snow at that location (FAC₁₀). The three purple circles indicate the locations of the case studies discussed in Sect. 4. Dashed lines represent 500 m elevation contours, the blue solid line the contiguous ice sheet margin.

With the newly adopted parametrizations, the simulation of FAC in dry locations has significantly improved (Fig. 5). The mean difference between the modelled and observed FAC (bias) has decreased from 0.61 to 0.41 m. Simultaneously, the root of the mean square of the difference between the modelled and observed FAC (RMSE) of all cores has decreased from 2.16 to 1.39 m. There are 39 locations with FAC > 15 m, which are all relatively dry. For these locations, the root mean squared error

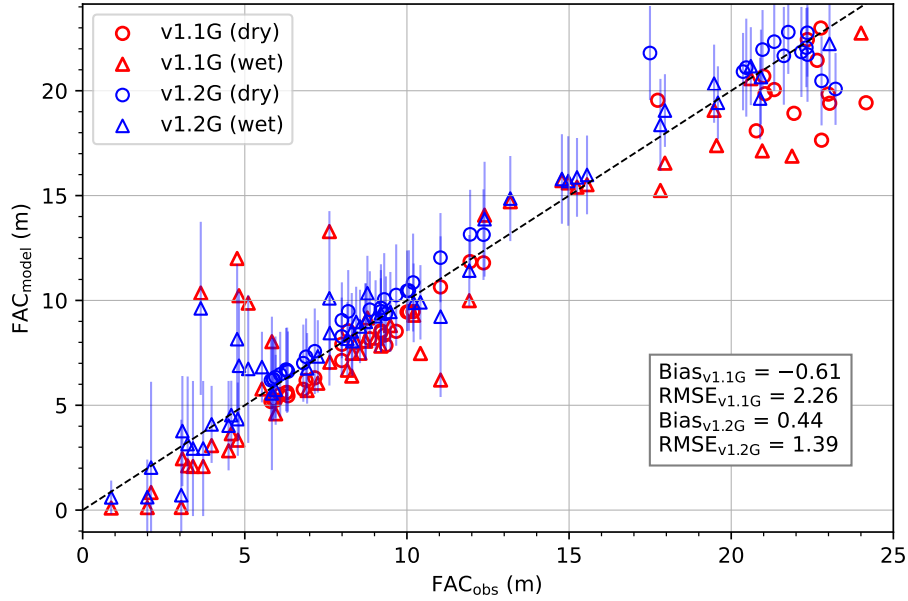


Figure 5. Modelled vs observed firm air content in metres. Dry locations are indicated with circles whereas wet locations are indicated with triangles. A location is labelled as dry if it experiences 5% less melt than accumulation during the spin-up period. The blue lines indicate the uncertainty in the v1.2G results.

315 (RMSE) decreased from 1.68 to 1.11 m (-34%). The improvement is more modest for low FAC locations, where the previous underestimation has now become a small overestimation. This can be attributed to the new fresh snow density parameterization, which results in lower densities especially close to the surface. For these 53 locations, the RMSE decreased from 2.60 to 1.57 m (-40%). Eq. (2) leads to a lower surface density, which in turn leads to a higher FAC. Simultaneously, a higher densification rate leads to a lower FAC, which suggests that the improvement in the modelled FAC stems mostly from the new fresh snow
 320 density parametrization, whereas the new densification rate ensures that the firm profile is modelled correctly at greater depths.

As mentioned in Sect. 2.1.1, Fausto et al. (2018) suggested using a constant density of 315 kg m^{-3} instead of using a temperature dependent formulation. Here, we analyse the model's performance when using a constant fresh snow density of 315 kg m^{-3} and compare that to the model's performance when using Eq. 2. We do this by comparing the RMSE in the FAC. Moreover, we define a core-specific RMSE in firm density, Φ , as an additional metric to quantify the error in the modelled
 325 vertical density profile:

$$\Phi = \sqrt{\frac{1}{L_z} \sum_i^{n_z} (\rho_{model,i} - \rho_{obs,i})^2} \quad (10)$$

With L_z the length of the core. This error quantifies the RMSE in the profile when comparing the modelled profile to the observations. The mean Φ then quantifies the mean performance of the model, and gives a slightly different result than the

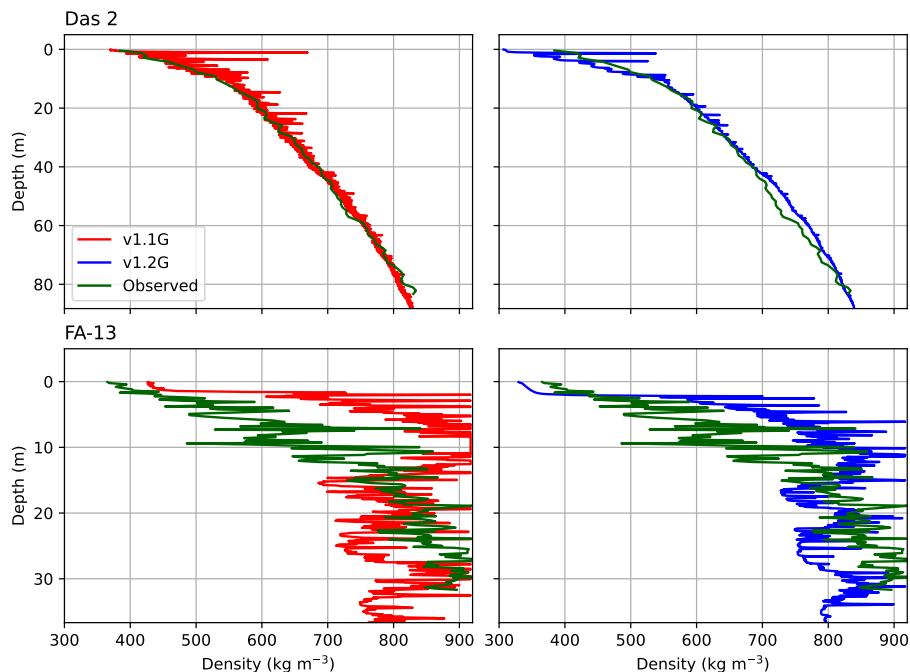


Figure 6. Density profiles for v1.2G (left) and v1.1G (right) model settings at Das 2 (top) and FA-13 (bottom).

RMSE in the FAC. The RMSE in FAC decreased from 2.26 m in v1.1G, to 1.39 m in v1.2G, where the surface snow density
 330 depends on annual mean temperatures. When employing a constant density of of 315 kg m^{-3} the RMSE is slightly higher:
 1.44 m. Similarly, the mean Φ of all density profiles decreased from $2.1 \cdot 10^3 \text{ kg m}^{-3}$ to $2.0 \cdot 10^3$ when using surface snow
 density that depends on annual mean temperatures and $1.9 \cdot 10^3 \text{ kg m}^{-3}$ when using a constant density respectively. These
 results show that including temperature as a predictor for the surface density does improve model performance, but only for
 FAC, not for Φ . Thus, we opt for the temperature dependent formulation, since this also allows capturing the effect of long-term
 335 temperature trends on the surface density.

Fig. 6 shows observed and modelled density profiles at Das 2 and FA-13, sites with large and small FAC respectively. Das
 2 is a dry location, with very little melt (4 mm w.e.yr^{-1}) and changes to its profile whereas FA-13 experiences strong melt
 ($406 \text{ mm w.e.yr}^{-1}$). The aquifer site was selected because its facies represent a distinct climatological zone on the GrIS, with
 a combination of high melt and high accumulation, which we expect will results in distinct firm characteristics. Standing water
 is not allowed in IMAU-FDM v1.2G, while this is known to occur at firm aquifer sites (Koenig et al. (2014); Miège et al.
 (2016); Montgomery et al. (2017); Miller et al. (2020)), so that modelled liquid water content remains a qualitative rather than
 340 quantitative estimate. In spite of this, it has previously been shown that the model accurately reproduces the spatial distribution
 of aquifers (Forster et al. (2014)), from which we conclude that first order processes that determine temperature and pore space
 (FAC) are sufficiently represented. At both sites, the changes made in v1.2G improved the modelled density-depth profile,
 345 with a more realistic shape and reduced variability. It increases the pore space and brings simulated FAC in better agreement

with the observed density profile. For both locations, the modelled FAC has improved: the bias at Summit has decreased from +1.3 m to -1.0 m and at FA-13 the bias has decreased from -2.2 to +0.3 m. Simultaneously, the Φ at both locations has remained nearly identical: an increase of 2.2 and 0.1 % at Summit and FA-13 respectively. One of the reasons for the increased performance is the change to a surface density parametrization that is based on annual mean temperature values instead of the temperature at the time of the snow event. This leads to greatly reduced "peaks" in the density profile, which is more in line with observations. For FA-13, the lower surface density also matches the upper 25 m of the density profile better.

3.2 Firn temperature

Modelled and measured 10 m firn temperatures at 31 locations are compared in Fig. 7. Model version 1.2G performs better than v1.1G, especially for the warmer locations with significant melt, which are mostly locations from Harper et al. (2012) in West Greenland. Here, the error at warmer locations has been significantly reduced: for locations with $T_{10} > -20$ °C, the mean RMSE decreased from 4.7 to 3.1 °C, respectively (-43%). A better representation of the density at those locations allows for more realistic refreezing and the associated enhanced latent heat release, increasing the temperature in melt-prone locations. Additionally, the lower conductivity due to the lower density leads to a less efficient cooling of the deeper snow during winter. In spite of the clear improvement, a cold-bias remains for some of these locations, which can be partly attributed to a cold-bias in the RACMO2 forcing. For the cold, low-melt locations ($T_{10} < -20$ °C), a persistent warm model bias remains. The remaining temperature bias can come from uncertainty in the forcing (surface temperature, liquid water input, snow accumulation, surface density) and uncertainties in the firn model (heat conduction, meltwater percolation, pore space availability, depth of refreezing). The model also does not include firn ventilation, which can warm or cool the firn depending on the season (Albert and Shultz (2002); Steger et al. (2017b)). Further research is needed to clarify the exact reasons for these remaining biases.

Fig. 8 compares the observed temperature profiles of Summit and Dye-2 in winter and summer with the results from IMAU-FDM v1.1G and v1.2G. Similarly to what was found in Fig. 7, Summit, which is a dry and cold location has a warm bias whereas Dye-2, which is relatively mild and wet, has a cold bias. For both locations the new surface density parameterization has decreased the density in the upper layers. This in turn leads to a lower thermal conductivity since the thermal conductivity increases monotonically with density (Fig. 3). Therefore, heat diffuses slower in the upper layers, increasing the temperature gradient there, which can be seen clearly at Summit.

Dye-2 now clearly shows a temperature maximum at the depth at which refreezing occurs in contrast to v1.1G. This is also attributed to a decrease in the thermal conductivity: previously, heat generated by refreezing was able to more rapidly diffuse to greater depths or the surface, but now it remains "trapped" around the depth at which refreezing occurs. Another factor that contributes is that refreezing occurs at a greater depth than before, see Sect. 3.3. We deem the differences with observations of 1 to 2 °C at these locations acceptable in light of the potential uncertainties in both forcing and firn processes, as described above.

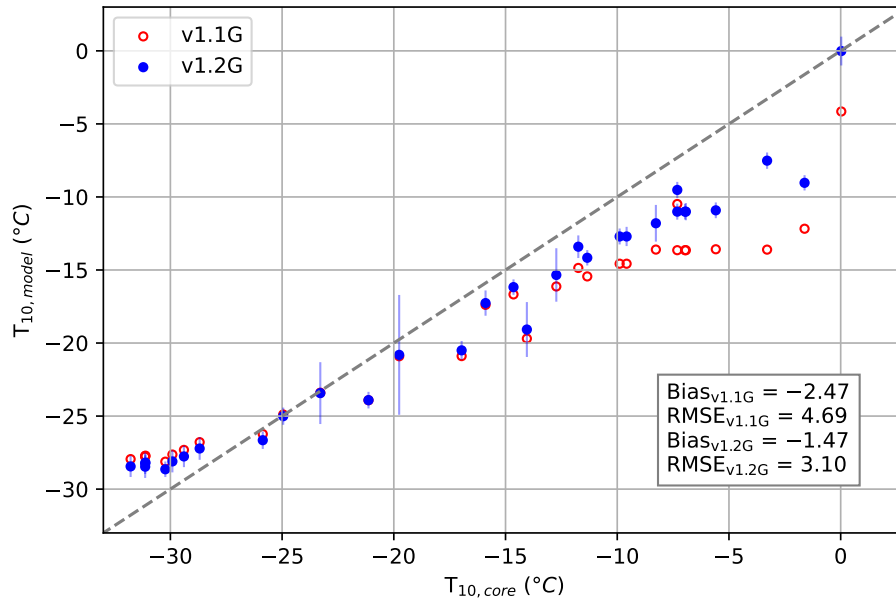


Figure 7. Modelled vs. observed temperature at 10 m depth (in °C) for 31 locations on the GrIS.

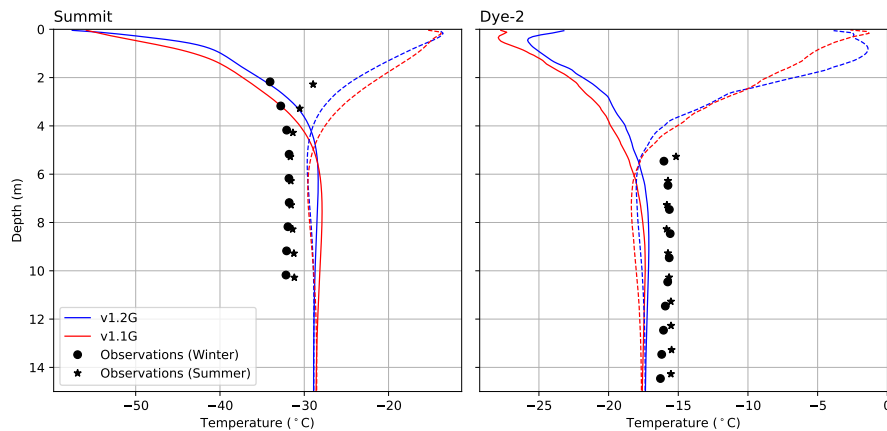


Figure 8. Comparison between observed temperature profiles vs. modelled profiles by v1.1G and v1.2G in summer (dashed lines) and winter (solid lines) at Summit in winter (9 March 2002) and summer (6 August 2002) and Dye-2 in the summer (10 August 2007) and winter (13 March 2007). The blue lines indicate the uncertainty in the v1.2G results.

3.3 Liquid water content

The liquid water percolation and retention schemes have not been updated, but the changes made to the parameterizations that impact density and temperature do influence water percolation, and therewith liquid water content (LWC), and these changes

380 are discussed here. Very few in-situ, vertically resolved observations of LWC are available. Here we used data from a recent study that used upward looking ground penetrating radar (upGPR) at Dye-2 in the higher percolation zone of the southwestern GrIS (2120 ma.s.l., see Fig. 4, Heilig et al. (2020)).

Fig. 9 compares the results of v1.1G and v1.2G against the observed evolution of the maximum penetration depth and LWC in the firn. The measurements reveal that the melt in 2016 at Dye-2 mostly occurred in four periods between July and October, 385 the timings of which are well captured in the RACMO2.3p2 forcing. Comparing v1.1G and v1.2G, the water penetration depth and LWC have both increased. This mainly reflects the decreased density in the upper layers at Dye-2. As discussed in the previous section, this leads to an increase in the temperature in the upper firn layer and stronger temperature gradients at Dye-2. The increase in temperature means that the water needs to percolate deeper into the firn pack before it can refreeze, which is reflected in the increased penetration depth. Simultaneously, the decrease of the surface density means that there is more pore 390 space near the surface that can retain irreducible water, explaining the increase in volume fraction. Overall, the penetration depth now agrees better with the observations, although in IMAU-FDM, the meltwater still refreezes too quickly in more shallow layers than observed. The RMSE of the penetration depth has decreased from 0.54 to 0.52 m. Similarly, the RMSE in the volume fraction has decreased from $3.41 \cdot 10^{-3}$ to $3.33 \cdot 10^{-3}$. Varying the irreducible water content by, e.g., multiplying Eq. 7 with a constant factor or using a constant volume or mass fraction, did not improve the result, and it was decided to leave 395 the liquid water scheme unchanged. The remaining deficiencies between the modelled and observed l.w.c. are in part due to still too low temperatures at Dye-2 compared to the measurements despite the improvements. This means that the liquid water will reach firn freezing point at a shallower depth. As mentioned in the previous section, remaining errors in the temperature profile come from a combination of uncertainties in the forcing (surface temperature, liquid water input, snow accumulation, surface density) and uncertainties in the firn model (heat conduction, meltwater percolation, pore space availability, depth of 400 refreezing).

4 Case studies

In this section we compare time series (1958-2020) of firn-induced surface elevation (i.e. firn depth) changes at three key locations: Summit in the cold and dry ice sheet interior, KAN-U in the relatively warm and dry southwestern percolation zone and FA-13 in the wet and relatively mild southeastern firn aquifer region (Koenig et al. (2014); Forster et al. (2014), as indicated 405 by the purple circles in Fig. 4). Table 2 provides geographical and climatological information of these locations.

4.1 Summit

Summit is located at the centre of the GrIS at a high elevation and therefore it experiences a low amount of snowfall and a negligible amount of rain and melt. The evolution of its elevation is therefore closely linked to changes in the temperature (higher temperatures lead to a higher compaction rate) and accumulation (higher accumulation leads to a thicker firn layer). 410 Panels a and c in Fig. 10 show how annual accumulation and mean annual skin temperature change over the course of the simulation period, as well as changes to the surface elevation and its velocity components, both for v1.1G and v1.2G.

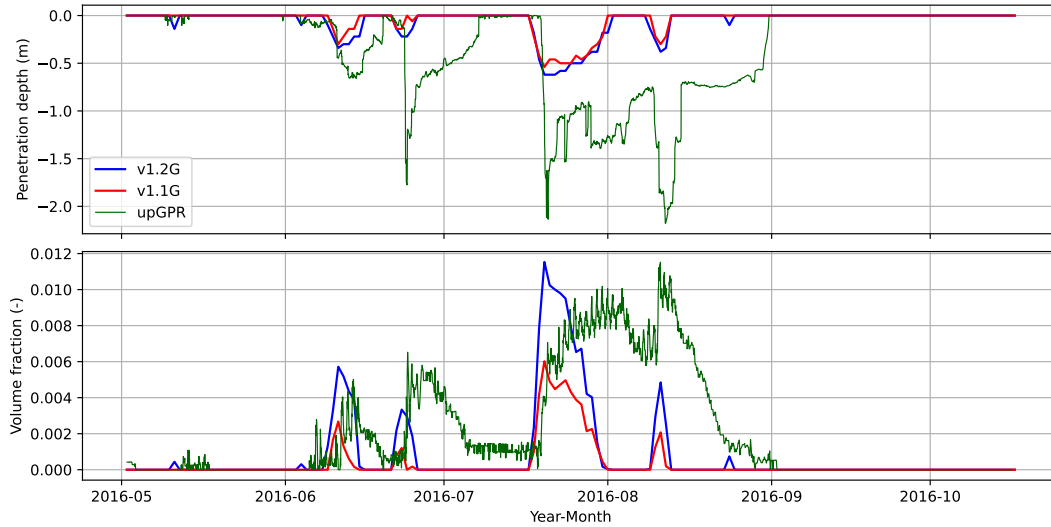


Figure 9. Comparison between the observed penetration depth (top) and volume fraction (bottom) of liquid water at Dye-2 with the results from v1.1G and v1.2G.

Table 2. Location and climate climate of the three case study sites. The annual mean accumulation are calculated over the whole simulation period (1957-2020).

	Lon. (°W)	Lat. (°N)	Elevation (m a.s.l.)	$T_{2\text{ m}}$ (°C)	Acc. (mm w.e.)	Melt (mm w.e.)
Summit	38.32	72.55	3281	-26.0	206	0
KAN-U	47.02	67.00	1840	-12.4	480	271
FA-13	39.04	66.18	1563	-7.0	986	496

At Summit, an 0.8 m elevation change between 1970 and 2000 is modelled (which equals $\sim 2.5 \text{ cm yr}^{-1}$ when divided by the number of years), with a slightly decreasing firn depth in the periods before and after. This can be explained by lower accumulation before about 1970 and after 2000, along with slightly increased temperatures since 2000. Differences in simulated surface elevation between v1.1G and v1.2G are small, in spite of the individual velocity components being different. As shown in panel g of Fig. 10, the interannual variability in firn depth is dominated by snowfall (v_{snow}), which is compensated mainly by steady firn compaction (v_{fc}). From this it follows that the slightly higher accumulation and lower temperature between ~ 1970 and 2000 caused the net upward surface velocity. Overall, the net vertical velocity of the surface is very similar between v1.1G and v1.2G, because both v_{snow} and v_{fc} have increased in magnitude almost equally. The new surface density parameterization (Eq. 1) leads to a lower surface density ($\sim 60 \text{ kg m}^{-3}$ lower at Summit), which in turn is compensated for by a higher densification rate in order to match the observed set of z_{550} and z_{830} values. Thus, with a lower surface density, the vertical upward velocity of the surface is higher, and the compaction velocity v_{fc} has also increase by an almost equal amount (~ 0.18

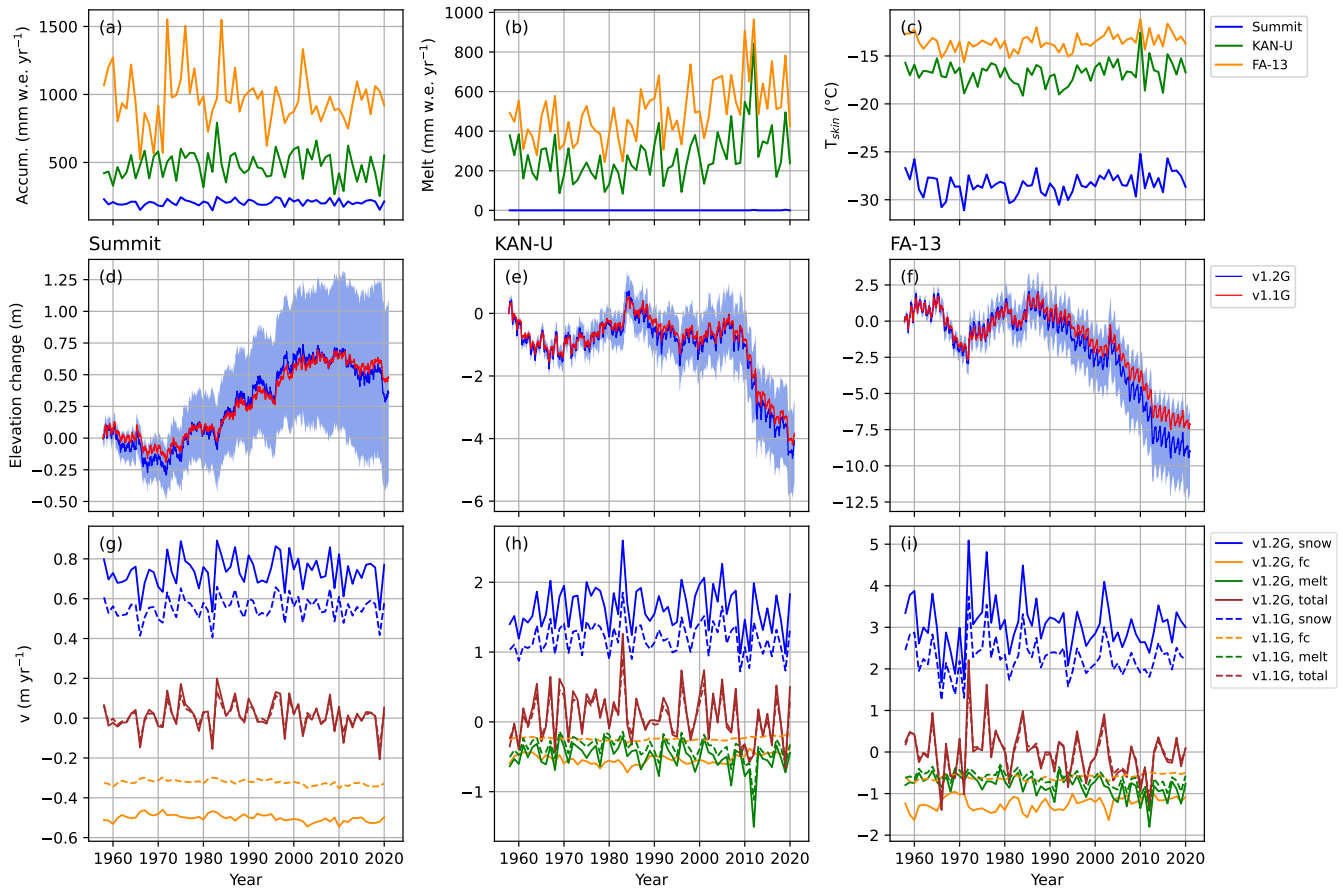


Figure 10. Time series of the total annual accumulation (a), total annual melt (b) and the annual mean skin temperature (c) at Summit, KAN-U and FA-13. Panels (d)-(f) show the net cumulative surface elevation change since the start of the simulation for these three locations. The blue area indicates the uncertainty in the v1.2G results. Finally, panels (g)-(j) show the mean annual velocity components that cause the elevation change.

m yr⁻¹). This explains why overall the total vertical velocity and the resulting surface elevation change does not differ much between v1.1G and v1.2G.

425 However, v1.2G does show larger seasonal and interannual oscillations in the firn depth. This is because v_{snow} and v_{fc} act on different timescales. v_{fc} is fairly constant in time and changes in tandem with the seasonal changes in temperature. v_{snow} on the other hand is much more variable, as snowfall is very episodic and highly variable at multiple time scales. This also implies that the firn model is now more sensitive to changes in the forcing, reacting more strongly to changes in accumulation and skin temperature.

430 4.2 KAN-U

Situated in the southwest and at a lower elevation, KAN-U is warmer than Summit and melting occurs every year during the summer, which greatly affects the firn properties at its location (Fig. 10b). The average influence of surface melt on firn depth changes (v_{melt} , Fig. 10h) is similar in magnitude and sign to the contribution from compaction (v_{fc}): it decreases the depth of the firn column and decreases its air content. At KAN-U, a 2.5 m thickening is modelled between 1970 and 1985. If we look
435 at the associated climate forcing, this can be explained by a relatively low amount of melt and a low temperature during this period. Between 2005 and 2020, a rapid decline (-20 cm yr⁻¹) is observed, which is associated with increased surface melt since 2005, as well as a slight increase in temperature and a reduction in accumulation. The most striking changes in elevation at KAN-U occurred in exceptional years, like 1983 as a very wet year, 2010 as a warm year, and 2012 as high-melt year.

When comparing the vertical surface velocities between v1.1G and v1.2G, we again see an increased accumulation velocity
440 v_{snow} , due to a lower fresh snow density, compensated for by a more negative compaction velocity resulting in a similar net velocity (v_{tot}). As accumulation decreased after 2005, the net effect is a slight surface lowering. Following significant warming and increased melt at this site (Fig. 10b, c), the contribution of v_{melt} to firn depth changes increases and that of v_{fc} decreases, making the former the dominant process leading to surface lowering at KAN-U. v_{melt} is also larger in magnitude in v1.2G because the melted snow at the surface is of a lower density, even though the amount of mass that melts is unchanged.

445 4.3 FA-13

FA-13, a site with a firn aquifer, experiences a warmer and wetter climate than KAN-U which leads to a rapid densification in the upper part of the firn column (Fig. 6). Here, the signal is dominated by large seasonal oscillations in firn depth of up to ~ 1 m yr⁻¹ between 1960 and 1985. From 1985 onwards, the firn depth decreases until 2012 at a higher rate in the updated than in the previous model (~ 0.35 vs. 0.25) m yr⁻¹.

450 For the vertical velocity components, a similar picture emerges at FA-13 as at KAN-U: v_{melt} becomes the dominant source of elevation lowering since 2005. The contribution of melt to surface elevation variations also becomes more important, because the melt itself increases and becomes more variable while the variability in accumulation decreases over time. At FA-13, the compaction is stronger and shows more interannual variability, in line with the larger interannual variability of the annual accumulation.

455 Both the variability and the magnitude of the melt is stronger in v1.2G. In the period 1990-2020, 8.5 m of thinning occurred
in v1.2G, compared to 6 m in v1.1G. Since the uppermost layers of snow are structurally less dense in v1.2G, enhanced surface
melt implies a stronger lowering of the surface, especially in strong melt years (10i).

5 Uncertainty analysis

In order to quantify the model uncertainty, we performed sensitivity tests in which the model settings, spin-up settings and
460 the RACMO forcing were varied one-by-one. The parametrizations for the snow density (Eq. 2) and the thermal conductivity
(Eq. 6) were varied by one standard error: 44 kg m^{-3} (Fausto et al. (2018)) and $0.05 \text{ W K}^{-1} \text{ m}^{-1}$ (Calonne et al. (2019)).
Following a similar procedure as Kuipers Munneke et al. (2015b), accumulation and melt during the spin-up has been increased
or decreased by 10%. Additionally, the temperature during spin-up was varied by $0.5 \text{ }^\circ\text{C}$. Similarly, we varied accumulation,
melt and temperature during the actual run by respectively 10% and $0.5 \text{ }^\circ\text{C}$. The spread in the results is indicative of the
465 sensitivity and accuracy of the model results. The resulting uncertainties are shown in Fig. 5 and 7 as error bars and in Fig. 10
as a shaded band around the elevation change signal.

These error margins do not include the uncertainty caused by missing physical processes in the model. For example, the
lack of deep water percolation may cause additional errors at wet locations. From these tests, it turns out that the uncertainty in
the modelled FAC (Fig. 5), is mainly caused by uncertainties in the surface snow density, skin temperature and accumulation.
470 However, the relative importance varies per location: wetter and warmer locations are more sensitive to the forcing.

The sensitivity of the modelled T_{10} (Fig. 7), scales almost one-to-one with the uncertainty imposed on the temperature
during the spin-up period and during the simulation period. However, for some locations such as KAN-U (located around -20
 $^\circ\text{C}$), the uncertainty is much larger, because melt at these locations turns out to be especially susceptible to a slightly higher
skin temperature. Simultaneously, T_{10} at these locations is very susceptible to a small increase in the amount of meltwater.
475 This combination makes these error bars larger. Remaining biases in the results are most likely due to missing physics in the
handling of liquid water percolation.

The blue shaded area in Fig. 10 shows the uncertainty in the firn depth at Summit, KAN-U and FA-13. This uncertainty
grows almost linearly over time. At Summit, the cumulative uncertainty at the end of 2020 is in the same order of magnitude
as the signal itself. These uncertainties are dominated by uncertainties during the spin-up period. We found that the elevation
480 change is sensitive to the initialised firn profile and spinning up the model with a slightly altered climate will result in a drift
in the elevation change. We used the period 1960-1980 as a reference climate during the spin-up. However, this climate is
not exactly representative of the firn's history and this thus introduces an error. Hawley et al. (2020) found that the mean
surface velocity at Summit equals 1.9 cm yr^{-1} during the period 2008-2018. IMAU-FDM v1.2G reports a small decrease of
 0.2 cm yr^{-1} , with an uncertainty of 3.2 cm yr^{-1} , indicating no significant trend. For the wetter and warmer locations KAN-U
485 and FA-13, the errors are larger in the absolute sense, but relatively smaller.

6 Summary and outlook

Temporal and spatial variability in firn layer thickness is highly relevant for studying the mass balance of the Greenland ice sheet (GrIS), because it directly impacts its refreezing efficiency. Moreover, firn thickness change is an important component of surface elevation change, and improved knowledge is required to accurately convert remotely sensed GrIS volume to mass changes. In this paper, we presented improvements in the offline version of the IMAU firn densification model (IMAU-FDM v1.2G), forced by three-hourly output of the regional climate model RACMO2.3p2. Taking advantage of improved climate forcing and newly available observations of surface and subsurface firn density and temperature, the improvements are systematically implemented in the parametrizations of surface density, dry snow densification and thermal conductivity. The treatment of liquid water is not changed, owing to a lack of sufficient observations to justify changes in the current configuration.

The updated model predicts higher firn air content (FAC), which at three selected sites in the interior GrIS and in the southwestern and southeastern percolation zone results in a larger sensitivity of firn thickness to intra- and interannual variations in snowfall, melt and temperature. As an important consequence of a change in fresh snow density parameterization, the inter- and intra-annual variations in elevation have increased, owing to an increased sensitivity to changes in its forcing. In a warmer climate, firn thinning owing to increased surface melt becomes increasingly important at the marginal sites, both in the mean and as a component of interannual variability. Future applications of the improved model include a full GrIS assessment of contemporary and future firn mass and thickness changes, as well as explaining areas where firn aquifers and ice slabs currently occur, and their future changes.

Code availability. The code of IMAU-FDM v1.2G used in this project is available on GitHub at <https://github.com/brils001/IMAU-FDM> and at Zenodo (<https://zenodo.org/record/5172513>, Brils et al. (2021)).

Data availability. J. E. Box, E. Mosley-Thompson, J. R. McConnell, K. Steffen, J. T. Harper and S. B. Das provided us with some of the firn core data that has been used to calibrate and validate IMAU-FDM. The rest of the firn cores were obtained from the SUMup dataset (Montgomery et al. (2018)). A list of all firn cores used and corresponding references can be found in the Supplementary Material. Firn temperatures are obtained from Vandecrux (2020), Polashenski et al. (2014) and Harper et al. (2012). The upGPR data of the liquid water measurements at Dye-2 are available from Heilig et al. (2018).

Author contributions. MB, PKM, WJvdB and MRvdB started this project, decided on its scope, which parts of the model required further development and interpreted the results. MB performed the model simulations, implemented the changes to the model, comparisons and led the writing of the manuscript. All authors contributed to discussions on the manuscript.

Competing interests. The authors declare that they have no conflict of interest.

Acknowledgements. This work was carried out under the program of the Netherlands Earth System Science Centre (NESSC), financially supported by the Ministry of Education, Culture and Science (OCW grant no. 024.002.001). We acknowledge ECMWF for computational time on their supercomputers.

References

- Albert, M. R. and Shultz, E. F.: Snow and firn properties and air-snow transport processes at Summit, Greenland, *Atmospheric Environment*, 36, 2789–2797, [https://doi.org/10.1016/S1352-2310\(02\)00119-X](https://doi.org/10.1016/S1352-2310(02)00119-X), 2002.
- 520 Anderson, E.: A point energy and mass balance model, Tech. Rep. D24, National Weather Office, https://repository.library.noaa.gov/view/noaa/6392/noaa_{_}6392_{_}, 1976.
- Arthern, R. J., Vaughan, D. G., Rankin, A. M., Mulvaney, R., and Thomas, E. R.: In situ measurements of Antarctic snow compaction compared with predictions of models, *Journal of Geophysical Research: Earth Surface*, 115, 1–12, <https://doi.org/10.1029/2009JF001306>, 2010.
- 525 Ashmore, D. W., Mair, D. W., and Burgess, D. O.: Meltwater percolation, impermeable layer formation and runoff buffering on Devon Ice Cap, Canada, *Journal of Glaciology*, 66, 61–73, <https://doi.org/10.1017/jog.2019.80>, 2019.
- Banta, J. R. and McConnell, J. R.: Annual accumulation over recent centuries at four sites in central Greenland, *Journal of Geophysical Research Atmospheres*, 112, 1–9, <https://doi.org/10.1029/2006JD007887>, 2007.
- Bezeau, P., Sharp, M., Burgess, D., and Gascon, G.: Firn profile changes in response to extreme 21st-century melting at Devon Ice Cap, Nunavut, Canada, *Journal of Glaciology*, 59, 981–991, <https://doi.org/10.3189/2013JoG12J208>, 2013.
- 530 Box, J. E., Cressie, N., Bromwich, D. H., Jung, J. H., Van den Broeke, M., Van Angelen, J. H., Forster, R. R., Miège, C., Mosley-Thompson, E., Vinther, B., and McConnell, J. R.: Greenland ice sheet mass balance reconstruction. Part I: Net snow accumulation (1600–2009), *Journal of Climate*, 26, 3919–3934, <https://doi.org/10.1175/JCLI-D-12-00373.1>, 2013.
- Braithwaite, R., Pfeffer, W., Blatter, H., and Humphrey, N.: Meltwater refreezing in the accumulation area of the Greenland ice sheet: Pâkitsoq, summer 1991, *Rapport Grønlands Geologiske Undersøgelse*, 155, 13–17, <https://doi.org/10.34194/rapggv.v155.8172>, 1992.
- 535 Brandt, R. E. and Warren, S. G.: Solar-heating rates and temperature profiles in Antarctic snow and ice, *Journal of Glaciology*, 39, 99–110, <https://doi.org/10.1017/S0022143000015756>, 1993.
- Brils, M., Kuipers Munneke, P., Van de Berg, W. J., and Van den Broeke, M.: IMAU-FDM v1 GDM release, <https://doi.org/10.5281/ZENODO.5172513>, 2021.
- 540 Brun, E., David, P., Sudul, M., and Brunot, G.: A numerical model to simulate snow-cover stratigraphy for operational avalanche forecasting, *Journal of Glaciology*, 38, 13–22, <https://doi.org/10.3189/S0022143000009552>, 1992.
- Calonne, N., Milliancourt, L., Burr, A., Philip, A., Martin, C. L., Flin, F., and Geindreau, C.: Thermal Conductivity of Snow, Firn, and Porous Ice From 3-D Image-Based Computations, *Geophysical Research Letters*, 46, 13 079–13 089, <https://doi.org/10.1029/2019GL085228>, 2019.
- 545 Charalampidis, C., Van As, D., Box, J. E., Van den Broeke, M. R., Colgan, W. T., Doyle, S. H., Hubbard, A. L., MacFerrin, M., Machguth, H., and P. Smeets, C. J.: Changing surface-atmosphere energy exchange and refreezing capacity of the lower accumulation area, West Greenland, *Cryosphere*, 9, 2163–2181, <https://doi.org/10.5194/tc-9-2163-2015>, 2015.
- Coble, R. L.: Diffusion models for hot pressing with surface energy and pressure effects as driving forces, *Journal of Applied Physics*, 41, 4798–4807, <https://doi.org/10.1063/1.1658543>, 1970.
- 550 Coléou, C. and Lesaffre, B.: Irreducible water saturation in snow: experimental results in a cold laboratory, *Annals of Glaciology*, 26, 64–68, <https://doi.org/10.3189/1998aog26-1-64-68>, 1998.
- Cuffey, K. and Paterson, W.: *The physics of glaciers*, vol. 57, fourth edn., <https://doi.org/doi.org/10.3189/002214311796405906>, 2011.

- Enderlin, E. M., Howat, I. M., Jeong, S., Noh, M.-J., Van Angelen, J. H., and van den Broeke, M. R.: An improved mass budget for the Greenland ice sheet, *Geophysical Prospecting*, pp. 6413–6419, <https://doi.org/10.1002/2014GL061184>. Received, 2014.
- 555 Fausto, R. S., Box, J. E., Vandecrux, B., van As, D., Steffen, K., MacFerrin, M. J., Machguth, H., Colgan, W., Koenig, L. S., McGrath, D., Charalampidis, C., and Braithwaite, R. J.: A Snow Density Dataset for Improving Surface Boundary Conditions in Greenland Ice Sheet Firn Modeling, *Frontiers in Earth Science*, 6, <https://doi.org/10.3389/feart.2018.00051>, 2018.
- Forster, R. R., Box, J. E., van den Broeke, M. R., Miège, C., Burgess, E. W., van Angelen, J. H., Lenaerts, J. T. M., Koenig, L. S., Paden, J., Lewis, C., Gogineni, S. P., Leuschen, C., and McConnell, J. R.: Extensive liquid meltwater storage in firn within the Greenland ice sheet, 560 *Nature Geoscience*, 7, 95–98, <https://doi.org/10.1038/ngeo2043>, 2014.
- Gascon, G., Sharp, M., Burgess, D., Bezeau, P., and Bush, A. B.: Changes in accumulation-area firn stratigraphy and meltwater flow during a period of climate warming: Devon Ice Cap, Nunavut, Canada, *Journal of Geophysical Research: Earth Surface*, 118, 2380–2391, <https://doi.org/10.1002/2013JF002838>, 2013.
- Hanna, E., McConnell, J., Das, S., Cappelen, J., and Stephens, A.: Observed and modeled Greenland Ice Sheet snow accumulation, 1958–565 2003, and links with regional climate forcing, *Journal of Climate*, 19, 344–358, <https://doi.org/10.1175/JCLI3615.1>, 2006.
- Harper, J., Humphrey, N., Pfeffer, W. T., Brown, J., and Fettweis, X.: Greenland ice-sheet contribution to sea-level rise buffered by meltwater storage in firn, *Nature*, 491, 240–243, <https://doi.org/10.1038/nature11566>, 2012.
- Hawley, R. L., Neumann, T. A., Stevens, C. M., Brunt, K. M., and Sutterley, T. C.: Greenland Ice Sheet Elevation Change: Direct Observation of Process and Attribution at Summit, *Geophysical Research Letters*, 47, 1–8, <https://doi.org/10.1029/2020GL088864>, 2020.
- 570 Heilig, A., Eisen, O., MacFerrin, M., Tedesco, M., and Fettweis, X.: Seasonal monitoring of melt and accumulation within the deep percolation zone of the Greenland Ice Sheet and comparison with simulations of regional climate modeling, *Cryosphere*, 12, 1851–1866, <https://doi.org/10.5194/tc-12-1851-2018>, 2018.
- Heilig, A., Eisen, O., Schneebeli, M., MacFerrin, M., Stevens, C. M., Vandecrux, B., and Steffen, K.: Relating regional and point measurements of accumulation in southwest Greenland, *The Cryosphere*, 14, 385–402, <https://doi.org/10.5194/tc-14-385-2020>, 2020.
- 575 Helsen, M. M., Van den Broeke, M. R., Van De Wal, R. S., Van De Berg, W. J., Van Meijgaard, E., Davis, C. H., Li, Y., and Goodwin, I.: Elevation changes in antarctica mainly determined by accumulation variability, *Science*, 320, 1626–1629, <https://doi.org/10.1126/science.1153894>, 2008.
- Herron, M. M. and Langway, C. C.: Firn densification: an empirical model., *Journal of Glaciology*, 25, 373–385, <https://doi.org/10.1017/S0022143000015239>, 1980.
- 580 Horlings, A. N., Christianson, K., Holschuh, N., Stevens, C. M., and Waddington, E. D.: Effect of horizontal divergence on estimates of firn-air content, *Journal of Glaciology*, 67, 287–296, <https://doi.org/10.1017/jog.2020.105>, 2021.
- Keenan, E., Wever, N., Dattler, M., Lenaerts, J. T., Medley, B., Kuipers Munneke, P., and Reijmer, C.: Physics-based SNOWPACK model improves representation of near-surface Antarctic snow and firn density, *Cryosphere*, 15, 1065–1085, <https://doi.org/10.5194/tc-15-1065-2021>, 2021.
- 585 Koenig, L., Box, J., and Kurtz, N.: Improving surface mass balance over ice sheets and snow depth on sea ice, *Eos*, 94, 100, <https://doi.org/10.1002/2013EO100006>, 2013.
- Koenig, L. S., Miège, C., Forster, R. R., and Brucker, L.: Initial in situ measurements of perennial meltwater storage in the Greenland firn aquifer, *Geophysical Research Letters*, 41, 81–85, <https://doi.org/10.1002/2013GL058083>, 2014.
- Kuipers Munneke, P., Ligtenberg, S. R., Suder, E. A., and Van den Broeke, M. R.: A model study of the response of dry and wet firn to 590 climate change, *Annals of Glaciology*, 56, 1–8, <https://doi.org/10.3189/2015AoG70A994>, 2015a.

- Kuipers Munneke, P., Ligtenberg, S. R. M., Noël, B. P. Y., Howat, I. M., Box, J. E., Mosley-Thompson, E., McConnell, J. R., Steffen, K., Harper, J. T., Das, S. B., and van den Broeke, M. R.: Elevation change of the Greenland Ice Sheet due to surface mass balance and firn processes, 1960–2014, *The Cryosphere*, 9, 2009–2025, <https://doi.org/10.5194/tc-9-2009-2015>, 2015b.
- Ligtenberg, S. R., Helsen, M. M., and Van Den Broeke, M. R.: An improved semi-empirical model for the densification of Antarctic firn, *Cryosphere*, 5, 809–819, <https://doi.org/10.5194/tc-5-809-2011>, 2011.
- Ligtenberg, S. R. M., Kuipers Munneke, P., Noël, B. P. Y., and van den Broeke, M. R.: Brief communication: Improved simulation of the present-day Greenland firn layer (1960–2016), *The Cryosphere*, 12, 1643–1649, <https://doi.org/10.5194/tc-12-1643-2018>, 2018.
- Lundin, J. M., Stevens, C. M., Arthern, R., Buizert, C., Orsi, A., Ligtenberg, S. R., Simonsen, S. B., Cummings, E., Essery, R., Leahy, W., Harris, P., Helsen, M. M., and Waddington, E. D.: Firn Model Intercomparison Experiment (FirnMICE), *Journal of Glaciology*, 63, 401–422, <https://doi.org/10.1017/jog.2016.114>, 2017.
- MacFerrin, M., Machguth, H., van As, D., Charalampidis, C., Stevens, C. M., Heilig, A., Vandecrux, B., Langen, P. L., Mottram, R., Fettweis, X., den Broeke, M. R., Pfeffer, W. T., Moussavi, M. S., and Abdalati, W.: Rapid expansion of Greenland’s low-permeability ice slabs, *Nature*, 573, 403–407, <https://doi.org/10.1038/s41586-019-1550-3>, 2019.
- Machguth, H., MacFerrin, M., Van As, D., Box, J. E., Charalampidis, C., Colgan, W., Fausto, R. S., Meijer, H. A. J., Mosley-Thompson, E., and van de Wal, R. S. W.: Greenland meltwater storage in firn limited by near-surface ice formation, *Nature Climate Change*, 6, 390–393, <https://doi.org/10.1038/nclimate2899>, 2016.
- Magnusson, J., Wever, N., Essery, R., Helbig, N., Winstral, A., and Jonas, T.: Evaluating snow models with varying process representations for hydrological applications, *Water Resources Research*, 51, 2707–2723, <https://doi.org/10.1002/2014WR016498>, 2015.
- McConnell, J. R., Mosley-Thompson, E., Bromwich, D. H., Bales, R. C., and Kyne, J. D.: Interannual variations of snow accumulation on the Greenland Ice Sheet (1985–1996): New observations versus model predictions, *Journal of Geophysical Research Atmospheres*, 105, 4039–4046, <https://doi.org/10.1029/1999JD901049>, 2000.
- McMillan, M., Leeson, A., Shepherd, A., Briggs, K., Armitage, T. W., Hogg, A., Kuipers Munneke, P., van den Broeke, M., Noël, B., van de Berg, W. J., Ligtenberg, S., Horwath, M., Groh, A., Muir, A., and Gilbert, L.: A high-resolution record of Greenland mass balance, *Geophysical Research Letters*, 43, 7002–7010, <https://doi.org/10.1002/2016GL069666>, 2016.
- Miège, C., Forster, R. R., Brucker, L., Koenig, L. S., Solomon, D. K., Paden, J. D., Box, J. E., Burgess, E. W., Miller, J. Z., McNerney, L., Brautigam, N., Fausto, R. S., and Gogineni, S.: Spatial extent and temporal variability of Greenland firn aquifers detected by ground and airborne radars, *Journal of Geophysical Research: Earth Surface*, 121, 2381–2398, <https://doi.org/10.1002/2016JF003869>, 2016.
- Miller, O., Solomon, D. K., Miège, C., Koenig, L., Forster, R., Schmerr, N., Ligtenberg, S. R., Legchenko, A., Voss, C. I., Montgomery, L., and McConnell, J. R.: Hydrology of a Perennial Firn Aquifer in Southeast Greenland: An Overview Driven by Field Data, *Water Resources Research*, 56, <https://doi.org/10.1029/2019WR026348>, 2020.
- Montgomery, L., Koenig, L., and Alexander, P.: The SUMup dataset: Compiled measurements of surface mass balance components over ice sheets and sea ice with analysis over Greenland, *Earth System Science Data*, 10, 1959–1985, <https://doi.org/10.5194/essd-10-1959-2018>, 2018.
- Montgomery, L. N., Schmerr, N., Burdick, S., Forster, R. R., Koenig, L., Legchenko, A., Ligtenberg, S., Miège, C., Miller, O. L., and Solomon, D. K.: Investigation of firn aquifer structure in southeastern Greenland using active source seismology, *Frontiers in Earth Science*, 5, 1–12, <https://doi.org/10.3389/feart.2017.00010>, 2017.

- Mosley-Thompson, E., McConnell, J. R., Bales, R. C., Li, Z., Lin, P. N., Steffen, K., Thompson, L. G., Edwards, R., and Bathke, D.: Local to regional-scale variability of annual net accumulation on the Greenland ice sheet from PARCA cores, *Journal of Geophysical Research Atmospheres*, 106, 33 839–33 851, <https://doi.org/10.1029/2001JD900067>, 2001.
- 630 Mouginito, J., Rignot, E., Björk, A. A., van den Broeke, M., Millan, R., Morlighem, M., Noël, B., Scheuchl, B., and Wood, M.: Forty-six years of Greenland Ice Sheet mass balance from 1972 to 2018, *Proceedings of the National Academy of Sciences of the United States of America*, 116, 9239–9244, <https://doi.org/10.1073/pnas.1904242116>, 2019.
- Nghiem, S. V., Hall, D. K., Mote, T. L., Tedesco, M., Albert, M. R., Keegan, K., Shuman, C. A., DiGirolamo, N. E., and Neumann, G.: The extreme melt across the Greenland ice sheet in 2012, *Geophysical Research Letters*, 39, 6–11, <https://doi.org/10.1029/2012GL053611>,
635 2012.
- Noël, B., Van De Berg, W. J., Van Meijgaard, E., Kuipers Munneke, P., Van De Wal, R. S., and Van den Broeke, M. R.: Evaluation of the updated regional climate model RACMO2.3: Summer snowfall impact on the Greenland Ice Sheet, *Cryosphere*, 9, 1831–1844, <https://doi.org/10.5194/tc-9-1831-2015>, 2015.
- Noël, B., van de Berg, W. J., Lhermitte, S., Wouters, B., Machguth, H., Howat, I., Citterio, M., Moholdt, G., Lenaerts, J. T. M., and van den
640 Broeke, M. R.: A tipping point in refreezing accelerates mass loss of Greenland’s glaciers and ice caps, *Nature Communications*, 8, 14 730, <https://doi.org/10.1038/ncomms14730>, 2017.
- Noël, B., van de Berg, W. J., Lhermitte, S., Wouters, B., Schaffer, N., and van den Broeke, M. R.: Six Decades of Glacial Mass Loss in the Canadian Arctic Archipelago, *Journal of Geophysical Research: Earth Surface*, 123, 1430–1449, <https://doi.org/10.1029/2017JF004304>, 2018a.
- 645 Noël, B., van de Berg, W. J., van Wessem, J. M., van Meijgaard, E., van As, D., Lenaerts, J. T. M., Lhermitte, S., Kuipers Munneke, P., Smeets, C. J. P. P., van Ulft, L. H., van de Wal, R. S. W., and van den Broeke, M. R.: Modelling the climate and surface mass balance of polar ice sheets using RACMO2 – Part 1: Greenland (1958–2016), *The Cryosphere*, 12, 811–831, <https://doi.org/10.5194/tc-12-811-2018>, 2018b.
- Noël, B., van de Berg, W. J., Lhermitte, S., and van den Broeke, M. R.: Rapid ablation zone expansion amplifies north Greenland mass loss, *Science Advances*, 5, 2–11, <https://doi.org/10.1126/sciadv.aaw0123>, 2019.
650
- Noël, B., Jakobs, C. L., van Pelt, W. J., Lhermitte, S., Wouters, B., Kohler, J., Hagen, J. O., Luks, B., Reijmer, C. H., van de Berg, W. J., and van den Broeke, M. R.: Low elevation of Svalbard glaciers drives high mass loss variability, *Nature Communications*, 11, 1–8, <https://doi.org/10.1038/s41467-020-18356-1>, 2020.
- Orsi, A. J., Kawamura, K., Masson-Delmotte, V., Fettweis, X., Box, J. E., Dahl-Jensen, D., Clow, G. D., Landais, A., and Severinghaus, J. P.:
655 The recent warming trend in North Greenland, *Geophysical Research Letters*, 44, 6235–6243, <https://doi.org/10.1002/2016GL072212>, 2017.
- Pfeffer, W. T., Meier, M. F., and Illangasekare, T. H.: Retention of Greenland runoff by refreezing: Implications for projected future sea level change, *Journal of Geophysical Research*, 96, 22 117, <https://doi.org/10.1029/91JC02502>, 1991.
- Polashenski, C., Courville, Z., Benson, C., Wagner, A., Chen, J., Wong, G., Hawley, R., and Hall, D.: Observations of pro-
660 nounced Greenland ice sheet firn warming and implications for runoff production, *Geophysical Research Letters*, 41, 4238–4246, <https://doi.org/10.1002/2014GL059806>, 2014.
- Reid, R. C., Sherwood, T. K., and Street, R. E.: The Properties of Gases and Liquids, *Physics Today*, 12, 38–40, <https://doi.org/10.1063/1.3060771>, 1959.

- Robin, G. D. Q.: Seismic shooting and related investigations: Norwegian-British-Swedish Antarctic Expedition, 1949–1952, *Scientific Results*, 5,
- 670 Shepherd, A., Ivins, E., Rignot, E., Smith, B., van den Broeke, M., Velicogna, I., Whitehouse, P., Briggs, K., Joughin, I., Krinner, G., Nowicki, S., Payne, T., Scambos, T., Schlegel, N., A. G., Agosta, C., Ahlstrøm, A., Babonis, G., Barletta, V. R., Bjørk, A. A., Blazquez, A., Bonin, J., Colgan, W., Csatho, B., Cullather, R., Engdahl, M. E., Felikson, D., Fettweis, X., Forsberg, R., Hogg, A. E., Gallee, H., Gardner, A., Gilbert, L., Gourmelen, N., Groh, A., Gunter, B., Hanna, E., Harig, C., Helm, V., Horvath, A., Horwath, M., Khan, S., Kjeldsen, K. K., Konrad, H., Langen, P. L., Lecavalier, B., Loomis, B., Luthcke, S., McMillan, M., Melini, D., Mernild, S., Mohajerani, Y., Moore, P.,
- 675 Mottram, R., Mouginot, J., Moyano, G., Muir, A., Nagler, T., Nield, G., Nilsson, J., Noël, B., Ootaka, I., Pattie, M. E., Peltier, W. R., Pie, N., Rietbroek, R., Rott, H., Sandberg Sørensen, L., Sasgen, I., Save, H., Scheuchl, B., Schrama, E., Schröder, L., Seo, K. W., Simonsen, S. B., Slater, T., Spada, G., Sutterley, T., Talpe, M., Tarasov, L., van de Berg, W. J., van der Wal, W., van Wessem, M., Vishwakarma, B. D., Wiese, D., Wilton, D., Wagner, T., Wouters, B., and Wuite, J.: Mass balance of the Greenland Ice Sheet from 1992 to 2018, *Nature*, 579, 233–239,
- Steffen, C., Box, J., and Abdalati, W.: Greenland Climate Network: GC-Net, US Army Cold Regions Reattach and Engineering (CRREL), CRREL Special Report, pp. 98–103,
- Steger, C. R., Reijmer, C. H., van den Broeke, M. R., Wever, N., Forster, R. R., Koenig, L. S., Munneke, P. K., Lehning, M., Lhermitte, S.,
- 690 Ligtenberg, S. R., Miège, C., and Noël, B. P.: Firn meltwater retention on the greenland ice sheet: A model comparison, *Frontiers in Earth Science*, 5,
- van Dalum, C. T., van de Berg, W. J., Lhermitte, S., and van den Broeke, M. R.: Evaluation of a new snow albedo scheme for the Greenland
- 695 ice sheet in the Regional Atmospheric Climate Model (RACMO2), *The Cryosphere*, 14, 3645–3662,
- Van den Broeke, M., Bamber, J., Ettema, J., Rignot, E., Schrama, E., Van Berg, W. J. D., Van Meijgaard, E., Velicogna, I., and Wouters, B.:
- 700 Partitioning recent Greenland mass loss, *Science*, 326, 984–986, [29](https://doi.org/10.1126/science.1178176, 2009.</p>
</div>
<div data-bbox=)

- Van den Broeke, M. R., Enderlin, E. M., Howat, I. M., Kuipers Munneke, P., Noël, B. P., Jan Van De Berg, W., Van Meijgaard, E., and Wouters, B.: On the recent contribution of the Greenland ice sheet to sea level change, *Cryosphere*, 10, 1933–1946, <https://doi.org/10.5194/tc-10-1933-2016>, 2016.
- 705 Van Wessem, J. M., Steger, C. R., Wever, N., and Van den Broeke, M. R.: An exploratory modelling study of perennial firn aquifers in the Antarctic Peninsula for the period 1979–2016, *Cryosphere*, 15, 695–714, <https://doi.org/10.5194/tc-15-695-2021>, 2021.
- Vandecrux, B.: Firn temperatures and measurement depths at nine Greenland Climate Network (GC-Net) weather stations, 1998–2017, Arctic Data Center, <https://doi.org/10.18739/A2833N00P>, 2020.
- 710 Vandecrux, B., MacFerrin, M., MacHguth, H., Colgan, W. T., Van As, D., Heilig, A., Max Stevens, C., Charalampidis, C., Fausto, R. S., Morris, E. M., Mosley-Thompson, E., Koenig, L., Montgomery, L. N., Miège, C., Simonsen, S. B., Ingeman-Nielsen, T., and Box, J. E.: Firn data compilation reveals widespread decrease of firn air content in western Greenland, *Cryosphere*, 13, 845–859, <https://doi.org/10.5194/tc-13-845-2019>, 2019.
- Vandecrux, B., Fausto, R. S., van As, D., Colgan, W., Langen, P. L., Haubner, K., Ingeman-Nielsen, T., Heilig, A., Stevens, C. M., MacFerrin, M., Niwano, M., Steffen, K., and Box, J.: Firn cold content evolution at nine sites on the Greenland ice sheet between 1998 and 2017, *Journal of Glaciology*, pp. 1–12, <https://doi.org/10.1017/jog.2020.30>, 2020a.
- 715 Vandecrux, B., Mottram, R., L. Langen, P., S. Fausto, R., Olesen, M., Max Stevens, C., Verjans, V., Leeson, A., Ligtenberg, S., Kuipers Munneke, P., Marchenko, S., Van Pelt, W., R. Meyer, C., B. Simonsen, S., Heilig, A., Samimi, S., Marshall, S., MacHguth, H., MacFerrin, M., Niwano, M., Miller, O., I. Voss, C., and E. Box, J.: The firn meltwater Retention Model Intercomparison Project (RetMIP): Evaluation of nine firn models at four weather station sites on the Greenland ice sheet, *Cryosphere*, 14, 3785–3810, <https://doi.org/10.5194/tc-14-3785-2020>, 2020b.
- 720 Vionnet, V., Brun, E., Morin, S., Boone, A., Faroux, S., Le Moigne, P., Martin, E., and Willemet, J.-M.: The detailed snowpack scheme Crocus and its implementation in SURFEX v7.2, *Geoscientific Model Development*, 5, 773–791, <https://doi.org/10.5194/gmd-5-773-2012>, 2012.
- Zwally, H. J., Jun, L., Jay Zwally, H., and Jun, L.: Seasonal and interannual variations of firn densification and ice-sheet surface elevation at the Greenland summit, *Journal of Glaciology*, 48, 199–207, <https://doi.org/10.3189/172756502781831403>, 2002.